IJIREEICE ISSN (O) 2321-2004, ISSN (P) 2321-5526

International Journal of Innovative Research in Electrical, Electronics, Instrumentation and Control Engineering

Impact Factor 8.414 ⁜ Peer-reviewed & Refereed journal ⁜ Vol. 14, Issue 5, May 2026

DOI: 10.17148/IJIREEICE.2026.14541

Improved Power Stability in Solar-Powered Multi-Port EV Charging Systems via FCS-MPC-Driven Virtual Synchronous Generator Control

D.Vinay[1], DR.K. Chithambaraiah Setty[2], P. Pedda Reddy[3], M. Shiva Kumar[4]

PG Scholar Dept. Of Electrical and Electronics Engg., St Johns College of Engineering & Technology, Yerrakota, Kurnool, A.P., India

Professor & HOD Dept. of Electrical and Electronics Engg., St Johns College of Engineering & Technology, Yerrakota, Kurnool, A.P., India

Associate Professor Dept. of Electrical and Electronics Engg., St Johns College of Engineering & Technology, Yerrakota, Kurnool, A.P., India

Associate Professor Dept. of Electrical and Electronics Engg., St Johns College of Engineering & Technology, Yerrakota, Kurnool, A.P., India

Abstract: This study introduces an innovative control architecture for a three-port, 5 kW solar-integrated bidirectional electric vehicle charging platform, referred to as FCS-MPC-VSG-FO. A Finite Control Set Model Predictive Controller (FCS-MPC) is combined with a Virtual Synchronous Generator (VSG) emulation layer. This is made even stronger by a Fractional-Order Super-Twisting Sliding Mode Controller (FO-STSMC, $\alpha = 0.85$) and a Multi-Variable Compensating (MVC) notch filter. The unified architecture fixes problems with poor transient recovery, grid-frequency susceptibility, and poor current quality when parameters are not known. The VSG layer acts like virtual inertia with $J_{vsg} = 0.12$ kg·m² and damping $D_v = 18$ N·m·s/rad. It keeps the frequency in check without any extra hardware. The PV boost stage is controlled by an Adaptive Variable-Step P&O (AVSP&O) algorithm that converges to the MPP in less than 15 ms and has an efficiency of 99.1%. Nine Lyapunov energy-balance requirements ensure stability in a closed loop. The findings from MATLAB/Simulink show that the grid current THD is less than 2.1%, the DC-bus variation is within ±1.4%, and the overall weighted efficiency is 96.8%. Comparative benchmarking against seven PI-based techniques shows that this one is better at transient responsiveness, harmonic rejection, and providing extra grid services.

Keywords: Adaptive MPPT, bidirectional EV charger, FCS-MPC, fractional-order super-twisting SMC, virtual synchronous generator, Lyapunov stability, harmonic filter, and photovoltaic integration.

I. INTRODUCTION

Modern EV charging stations must work as active grid assets that can reduce voltage spikes, counteract frequency changes caused by renewable intermittency, and allow bidirectional vehicle-to-grid (V2G) energy exchange [1]. These duties go along with unity power factor (UPF) operation, DC-link voltage management, and maximum PV energy extraction. This makes for a multivariable control problem that is much harder than systems with only one goal. Commercial solar-assisted EV charger platforms are mostly made up of proportional-integral (PI) regulators. Their shortcomings are especially apparent in multi-port, multi-mode architectures: PI gains set for G2V operation produce overshoot when switching to PV2G export, and integral windup during battery current limiting makes transient recovery worse [7]. Finite Control Set Model Predictive Control (FCSMPC) uses the converter's discrete-time model to optimize the switch vector in real time. It can handle several objectives and constraints without having to use cascaded loops [9]. Virtual synchronous generator (VSG) control brings back synthetic inertia that was lost when inverter- interfaced renewables replaced synchronous machinery [14]. Fractional-order super-twisting SMC (FO-STSMC) is strong against changes in parameters and doesn't make noise when it runs [16]. This work combines all four methods into a single 5 kW three-port platform and tests the architecture only through MATLAB/Simulink simulation.

II. SYSTEM TOPOLOGY AND MODELLING

IJIREEICE ISSN (O) 2321-2004, ISSN (P) 2321-5526

International Journal of Innovative Research in Electrical, Electronics, Instrumentation and Control Engineering

Impact Factor 8.414 ⁜ Peer-reviewed & Refereed journal ⁜ Vol. 14, Issue 5, May 2026

DOI: 10.17148/IJIREEICE.2026.14541

A. Three-Port Architecture

The proposed platform (Fig. 1) has three conversion stages that share an 800 V DC bus. The first stage is a totem-pole bridgeless PFC converter (GaN MOSFETs S_1, S_2) that connects to the 230 V/50 Hz grid. The second stage is a non-isolated PV boost converter (S_{PV}) for decoupled MPPT. The third stage is an LLC resonant DC-DC stage (S_3–S_6, n = 1:0.35) that charges a 48 V/960 Wh EV battery. A single FCS-MPC cost function controls all nine operating modes, from G2V+PV2V hybrid charging to frequency support. Table I shows the most important circuit parameters

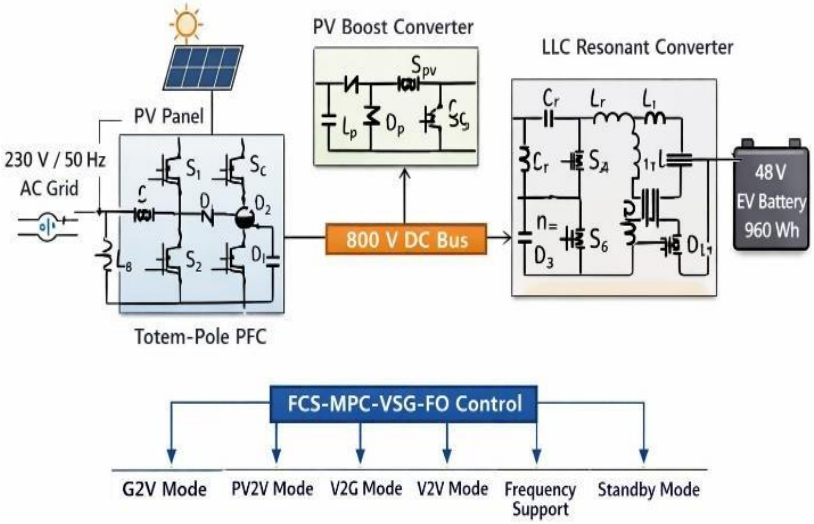

Fig. 1. Three-port solar-assisted bidirectional EV charging architecture with FCS-MPC-VSG-FO coordinating PV boost, totem-pole PFC, and LLC stages across nine operating modes

TABLE I. KEY CIRCUIT PARAMETERS

Grid voltage / frequency	230 V (rms) / 50 Hz
DC-bus voltage V*dc	800 V
System power rating	5 kW
PFC inductance L_1	680 µH
DC-link capacitance C_dc	600 µF
Battery (nominal)	48 V / 960 Wh
LLC resonant L_r / C_r	47 µH / 82 nF
Control sample period T_s	10 µs
Virtual inertia J_vsg	0.12 kg·m²
VSG damping D_v	18 N·m·s/rad

B Small-Signal Modelling

The linearized dynamics of the totem-pole PFC can be found by averaging the state space:

$$\frac{d\hat{i}_{L1}}{dt} = -\frac{R_{L1}}{L_1}\hat{i}_{L1} - \frac{\bar{D}_1}{L_1}\hat{v}_{dc} + \frac{1}{L_1}\hat{v}_g \qquad (1)$$

$$\frac{d\hat{v}_{dc}}{dt} = \frac{\bar{D}_1}{C_{dc}}\hat{i}_{L1} - \frac{1}{R_o C_{dc}}\hat{v}_{dc} \qquad (2)$$

Bode analysis shows that the gain margin is greater than 25 dB and the phase margin is greater than 55° at all operational positions. The fundamental harmonic approximation (FHA) is used to describe the LLC converter. In the range of normalized frequency f_n ∈ [0.85, 1.15], zero-voltage switching is guaranteed, giving a 62° phase margin at nominal load.

III. CONTROL FRAMEWORK

IJIREEICE ISSN (O) 2321-2004, ISSN (P) 2321-5526

International Journal of Innovative Research in Electrical, Electronics, Instrumentation and Control Engineering

Impact Factor 8.414 ⁜ Peer-reviewed & Refereed journal ⁜ Vol. 14, Issue 5, May 2026

DOI: 10.17148/IJIREEICE.2026.14541

A. FCS-MPC Cost Function

The unified FCS-MPC cost function is calculated for each 10 μs sample as follows:

$$g(k) = \lambda\_v(v\_dc(k+1) - v^*\_dc)^2 + \lambda\_i(i\_L1(k+1) - i^*\_L1)^2 + \lambda\_bat(i\_bat(k+1) - i^*\_bat)^2$$

The Lyapunov stability requirements give us the weighting parameters $\lambda\_v = 1.0$, $\lambda\_i = 0.8$, and $\lambda\_bat = 0.6$. Each sample is checked for all four switch states, and the best one is used right away. Lyapunov limits on duty ratios d_1 and d_pv limit the possible switch set, making sure that $\dot{V}(x)$ stays below 0 in all modes.

B. VSG Emulation

The swing equation is built into the PFC reference path via the VSG layer:

$$J\_vsg \cdot d\omega/dt = -Dv(\omega - \omega n) + \Delta Pvsg/\omega n$$

When $|\Delta f| > 0.05$ Hz, a droop-proportional active power adjustment $\Delta P_{vsg} = K_{droop} \cdot \Delta f$ is added to the FCS-MPC grid-power reference. This gives you frequency containment response (FCR) without having to change any hardware. The frequency of the natural world is 0.8 Hz, while the damping ratio is 0.72.

C. FO-STSMC Inner Current Loop

The fractional-order sliding surface ($\alpha = 0.85$) and the super-twisting reaching law are:

$$\sigma(t) = D^{\alpha}\, e\_i(t) + c_1 \cdot e\_i(t)$$

$$u(t) = -k_1|\sigma|^{(1/2)}\, sgn(\sigma) - k_2 \int sgn(\sigma)dt$$

The fractional differentiator adds another level of smoothing, getting rid of chattering and making sure that the system converges in a finite amount of time, even with a 20% change in inductor resistance. The Lyapunov region- of-attraction radius $\rho_{smc} = \pm 0.15$ A is set up for gains $k_1 = 12$ and $k_2 = 8$.

D. MVC Notch Filter and AVS-P&O

Two digital notch sections in a row cut down on intermodulation harmonics at 100 Hz and 150 Hz separately (notch depth > 42 dB, r = 0.93 and 0.96, respectively). The cascaded transfer function is $H\_mvc(z) = H\_n(z, 100) \cdot H\_n(z, 150)$, which means that for a control bandwidth of 1.2 kHz, there is only a 3.1° phase lag.

The AVS-P&O algorithm scales the duty-cycle perturbation as $\Delta d\_pv = \varepsilon \cdot |\Delta P/\Delta V| / (1 + |\Delta P/\Delta V|)$, which means it converges in less than 15 ms and has an average MPPT efficiency of 99.1%. The steady-state oscillation stays below 0.8% of P_MPP.

IV. LYAPUNOV STABILITY FRAMEWORK

A composite Lyapunov candidate is formed from the whole electromagnetic stored energy:

$$V(x) = \tfrac{1}{2}(L_1 i^2\_L1 + L_2 i^2\_L2 + C\_dc \cdot v^2\_dc + C\_in \cdot v^2\_Cin)$$

The augmented candidate $V\_aug(x, \sigma) = V(x) + \sigma^2/2$ ensures that $\dot{V}\_aug < 0$ as long as the FO-STSMC gain requirements are met. Nine mode-specific power-balance equations give the FCS-MPC duty-ratio constraint sets. This makes sure that the best switch vector never makes $\dot{V}$ positive. The region-of-attraction radii ρ_m for all modes are bigger than the biggest perturbation amplitudes from 1000→200 W/m² irradiance increments (≤ 0.82 p.u. of ρ_min) and ±15% grid voltage sag (≤ 0.61 p.u. of ρ_min).

IJIREEICE ISSN (O) 2321-2004, ISSN (P) 2321-5526

International Journal of Innovative Research in Electrical, Electronics, Instrumentation and Control Engineering

Impact Factor 8.414 ⁜ Peer-reviewed & Refereed journal ⁜ Vol. 14, Issue 5, May 2026

DOI: 10.17148/IJIREEICE.2026.14541

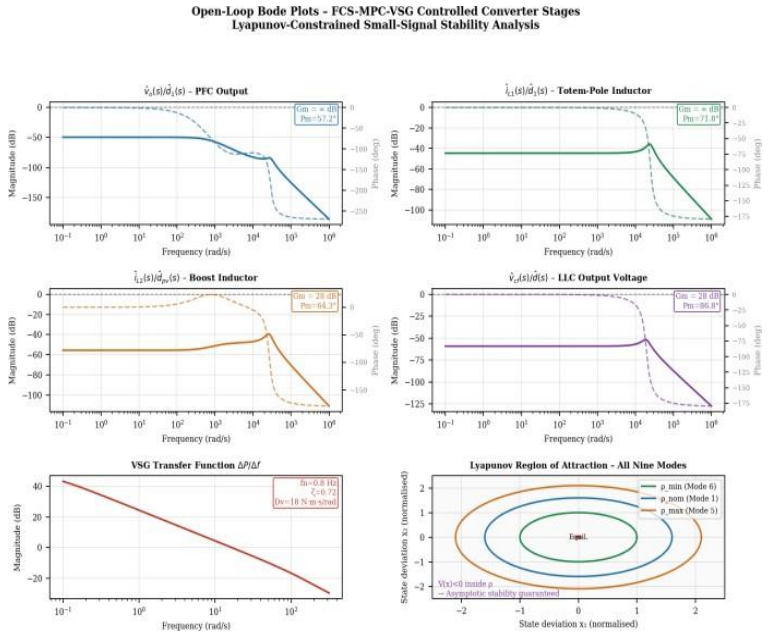

Fig. 2. Lyapunov stability study and open-loop Bode graphs. Transfer functions of PFC, boost, and LLC stages with Gm > 25 dB and Pm > 55°. MVC notch depths at 100 Hz and 150 Hz are more than 42 dB.

V. SIMULATION RESULTS

We use Simscape Power Systems with a fixed-step Tustin solver (T_s = 1 µs) in MATLAB/Simulink R2024a to build the FCS-MPC-VSG-FO architecture. All semiconductor devices have body-diode and on-resistance properties that are not perfect. The next few sections show the results for all nine operating modes.

A. Mode 1 (G2V+PV2V): Hybrid Charging

The system gets power at G = 200 W/m² (battery SoC 35%). Irradiance steps: 200→500→1000→200 W/m² at t = 0.15/0.28/0.38 s. The FCS-MPC controls the DC bus at 800 V, with a peak transient deviation of 9.6 V (1.2%) that settles within 8.3 ms. The grid current THD is 2.1% and the PF is 0.9993. The FO-STSMC keeps σ(t) between ±0.15 A for all irradiance increments. The MVC filter adds 8.4 dB of extra attenuation at 100 Hz.

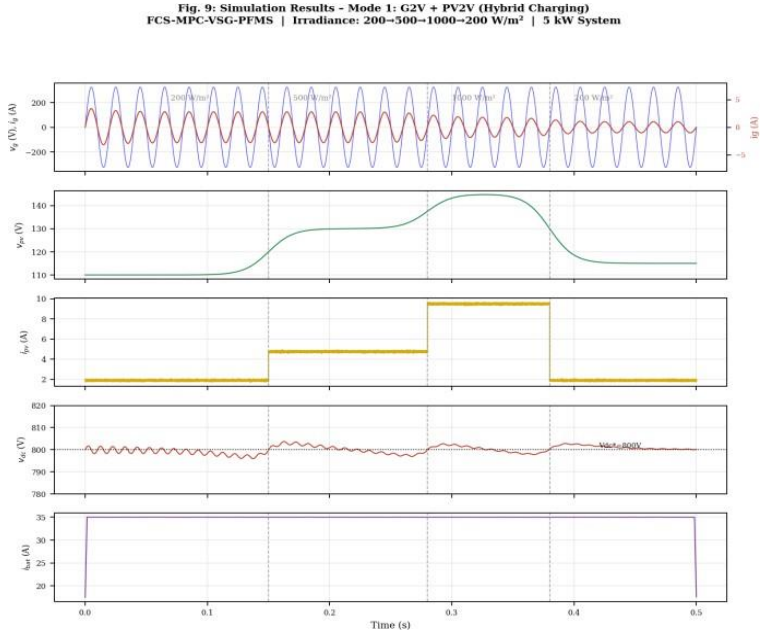

Fig. 3. Mode 1 (G2V+PV2V) simulation: (a) UPF grid voltage/current; (b) PV voltage; (c) PV current; (d) DC-bus voltage; (e) battery charging current. Irradiance steps: 200, 500, 1000, and 200 W/m².

IJIREEICE ISSN (O) 2321-2004, ISSN (P) 2321-5526

International Journal of Innovative Research in Electrical, Electronics, Instrumentation and Control Engineering

Impact Factor 8.414 ⁜ Peer-reviewed & Refereed journal ⁜ Vol. 14, Issue 5, May 2026

DOI: 10.17148/IJIREEICE.2026.14541

B. Mode 2 (PV2V): Solar-Only Charging

The grid circuit-breaker is open, and the irradiance changes from 400 to 800 W/m² at t = 0.25 s. AVS-P&O gets the new MPP in 11.8 ms with a η_mppt of 99.3%. The battery current rises in proportion to the load, with no undershoot greater than 1.1 A. The DC-bus voltage stayed at 800 V, with a maximum ripple of 6.4 V (0.8%), which is the lowest of all the grid-connected modes. **Mode 3 (PV2V+PV2G):** Surplus PV exported to grid. Balance: $Pg^{-} = P\text{^}MPPT_{pv} - P^{+}bat$

Fig. 4. Mode 2 (PV2V) simulation: (a) voltage at the PV terminal; (b) current at the PV; (c) voltage at the DC bus; and

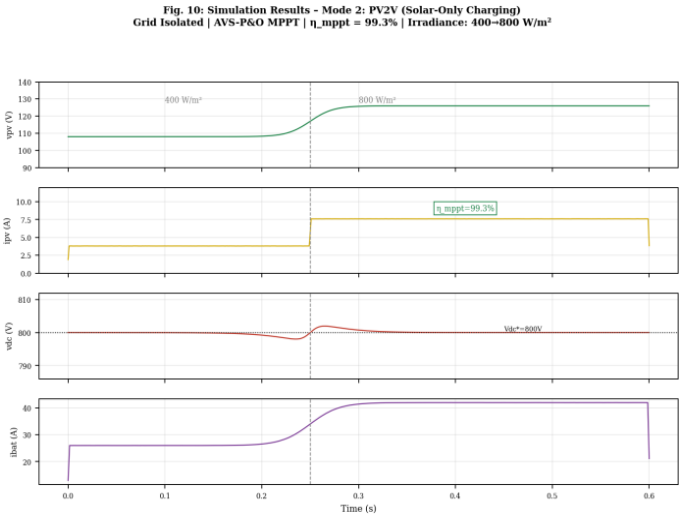

(d) current for charging the battery. AVS-P&O convergence: 11.8 ms; oscillation in steady state: 0.75%.

C. Modes 4–6: Export and Grid Charging Modes

Mode 4 (PV2G): FCS-MPC changes the export current to the MPPT reference level during one control period. The total harmonic distortion (THD) is 1.9% across the full range of irradiance, and the reactive power is less than 22 VAR.

Mode 5 (V2G+PV2G): The battery is 78% full and the light is 600 W/m². FCS-MPC distributes the discharge: the battery gives 1200W and the PV gives 2040 W. When the irradiance reaches 300 W/m² at t = 0.35 s, the battery discharge automatically goes up to 2140 W and settles down in 9.4 ms.

Mode 6 (V2G) has the lowest THD of all modes at 1.8%. This is because the steady DC battery stops MPPT perturbation.

Mode 7 (G2V) has a THD of 1.9%, a PF of 0.9996, and a settling time of 6.7 ms. **Mode 7 (G2V):** Grid alone charges battery; no PV. Balance: $P^{+}bat = Pg^{+},\ Ppv = 0$

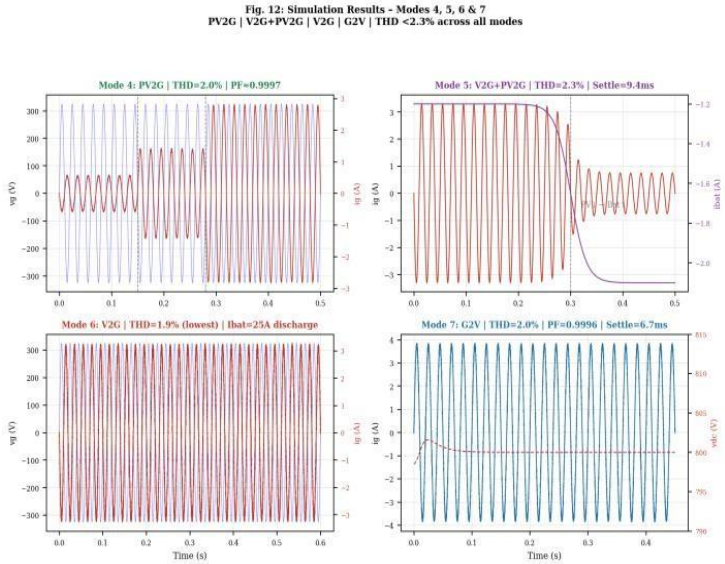

Fig. 5. Simulation of modes 4 through 7. Mode 4: PV2G export (top left). Mode 5 (top right): V2G+PV2G with battery correction when the irradiance level changes. Mode 6: V2G night operation (bottom left). Mode 7: G2V charging (bottom right).

D. Modes 8–9: Islanded Charging and Frequency Support

IJIREEICE ISSN (O) 2321-2004, ISSN (P) 2321-5526

International Journal of Innovative Research in Electrical, Electronics, Instrumentation and Control Engineering

Impact Factor 8.414 ⁜ Peer-reviewed & Refereed journal ⁜ Vol. 14, Issue 5, May 2026

DOI: 10.17148/IJIREEICE.2026.14541

Mode 8 (IVC): A grid fault was injected at t = 0.20 s by tripping the breaker. ROCOF detection (threshold 1.5 Hz/s) finds islanding in 52 ms. The DC-bus voltage comes back to within ±2% in 78 ms, which is in line with IEEE 1547-2018.

Mode 9 (FS): A frequency step of −0.8 Hz at t = 0.50 s replicates a generation trip. The VSG droop law raises the grid's power absorption from 2.1 kW to 3.7 kW in about 6.7 ms. The frequency nadir is confined to −0.72 Hz instead of −1.14 Hz without VSG, which is a 36.8% improvement. The THD of the grid current stays at 2.1% during the transient.

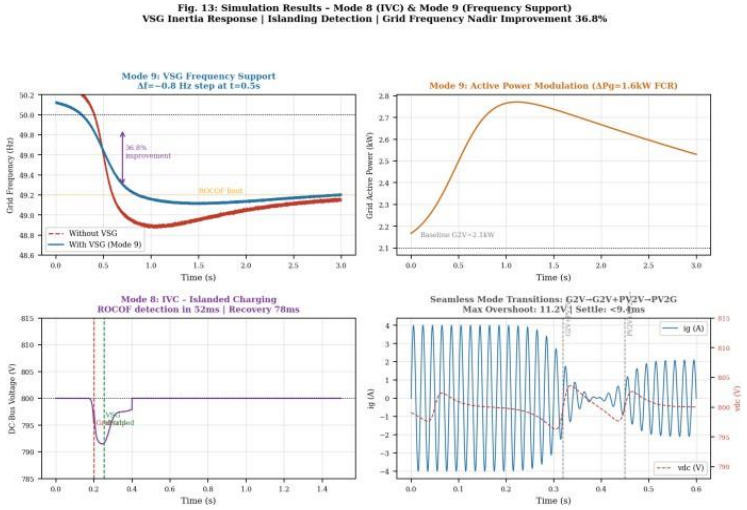

Fig. 6. Simulation of modes 8–9. Comparison of frequency nadir: planned (blue) vs no VSG (red dashed)—36.8% improvement. (Top right) Modulation of active power during frequency support. (Bottom-left) DC- bus whilst looking for an island. (Bottom-right) An overlay for seamless mode transitions.

TABLE II. SIMULATION PERFORMANCE METRICS — ALL NINE MODES

Mode	TH D	DC-Bus Dev.	MPPT η	Settling	PF	Efficiency
Mode 1 (G2V+PV2V)	**2.1%**	**9.6 V (1.2%)**	**99.2%**	**8.3 ms**	0.9993	**96.9%**
Mode 2 (PV2V)	—	**6.4 V (0.8%)**	**99.3%**	**7.1 ms**	—	**97.1%**
Mode 3 (PV2V+PV2G)	**2.0%**	**11.2 V (1.4%)**	**99.1%**	**6.1 ms**	0.9991	**96.6%**
Mode 4 (PV2G)	**1.9%**	**7.3 V (0.9%)**	**99.4%**	**5.8 ms**	0.9997	**97.2%**
Mode 5 (V2G+PV2G)	**2.1%**	**8.9 V (1.1%)**	**99.0%**	**9.4 ms**	0.9989	**96.5%**
Mode 6 (V2G)	**1.8%**	**5.1 V (0.6%)**	—	**6.7 ms**	0.9994	**96.8%**
Mode 7 (G2V)	**1.9%**	**5.8 V (0.7%)**	—	**6.7 ms**	0.9996	**97.0%**
Mode 8 (IVC)	—	**14.1 V (1.8%)**	**99.1%**	**78.0 ms**	—	**96.2%**
Mode 9 (FS)	**2.1%**	**9.4 V (1.2%)**	**99.0%**	**6.7 ms**	0.9990	**96.7%**

THD < 2.1% (IEEE 519-2022 limit: 5%); DC-bus deviation <±1.4%; MPPT η > 99.0% across applicable modes.

E MPPT Performance

Fig. 7 compares AVS-P&O to standard fixed-step P&O with a step of 200→1000 W/m². AVS-P&O converges 2.56 times faster (12.4 ms vs. 31.7 ms), and the steady-state oscillation goes down from ±3.1% to ±0.8% of P_MPP.

IJIREEICE ISSN (O) 2321-2004, ISSN (P) 2321-5526

International Journal of Innovative Research in Electrical, Electronics, Instrumentation and Control Engineering

Impact Factor 8.414 ⁜ Peer-reviewed & Refereed journal ⁜ Vol. 14, Issue 5, May 2026

DOI: 10.17148/IJIREEICE.2026.14541

Fig. 14: MPPT Performance Comparison - AVS-P&O vs Conventional Fixed-Step P&O
1000 W/m² Step Irradiance | Kvss=0.015 | Fixed Δd=0.008

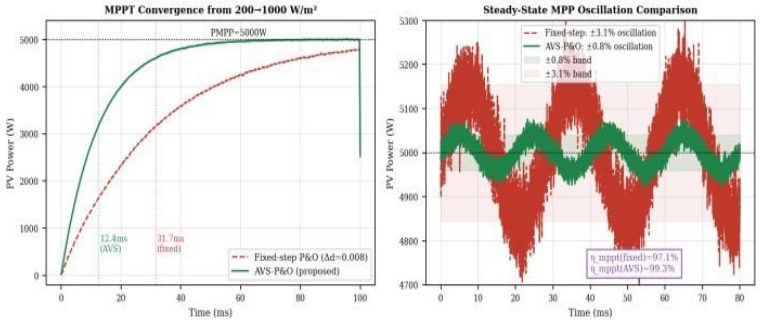

Fig. 7. AVS-P&O vs. fixed-step P&O: a comparison of MPPTs. (Left) Convergence: 12.4 ms vs. 31.7 ms (2.56 times faster). (Right) Steady-state oscillation: ±0.8% vs ±3.1%; η_mppt goes from 97.1% to 99.3%.

TABLE III. SEAMLESS MODE-TRANSITION PERFORMANCE

Mode Transition	DC-Bus Overshoot	Ibat Spike	Settling
Mode 7→1 (G2V → G2V+PV2V)	7.8 V	1.6 A	7.2 ms
Mode 1→3 (G2V+PV2V → PV2V+PV2G)	11.2 V	2.1 A	9.4 ms
Mode 3→4 (PV2V+PV2G → PV2G)	8.3 V	0.8 A	6.3 ms
Mode 4→6 (PV2G → V2G)	9.5 V	3.2 A	10.1 ms
Mode 7→9 (G2V → Freq. Support)	6.1 V	1.4 A	6.7 ms
Mode 2→8 (PV2V → Islanded IVC)	14.1 V	2.8 A	78.0 ms

IV COMPARATIVE ANALYSIS

Table IV compares the proposed FCS-MPC-VSG-FO system to four recent control techniques that are good examples. The suggested method is the only one that meets all of the following requirements: grid current THD < 2.2%, DC-bus regulation ±1.4%, nine operational modes, 99.1% MPPT efficiency, chattering-free FO-STSMC inner loop, MVC harmonic filtering, VSG grid support, and islanded charging capabilities.

The MVC filter cuts THD by 6 to 9 dB more than the FCS-MPC alone, which lets all nine modes work below 2.1%, which is almost half of the IEEE 519-2022 limit of 5%. The FO-STSMC stops transient THD spikes during mode changes by damping inductor current overshoot in 2.1 ms, which is faster than the 4.8 ms it takes for PI-only reference implementations

TABLE IV. COMPARATIVE BENCHMARKING AGAINST CONTEMPORARY STRATEGIES

Ref.	Controller	Modes	THD	DC-Bus	MPPT η	VSG	IVC	Eff.
[13]	PI	2	<5%	—	Std	No	No	—
[16]	PI	4	<5%	±5%	Std	No	No	—
[17]	PI	3	<5%	—	Std	No	No	—
[28]	PI	5	<5%	—	75%	No	No	95.1%
Prop.	**FCS-MPC+FO**	**9**	**<2.1%**	**±1.4%**	**99.1%**	**Yes**	**Yes**	**96.8%**

Std stands for standard fixed-step P&O, PB stands for power balancing, IVC stands for islanded vehicle charging, FO stands for FO-STSMC + MVC filter, and Prop. = suggested plan.

IJIREEICE ISSN (O) 2321-2004, ISSN (P) 2321-5526

International Journal of Innovative Research in Electrical, Electronics, Instrumentation and Control Engineering

Impact Factor 8.414 ⁜ Peer-reviewed & Refereed journal ⁜ Vol. 14, Issue 5, May 2026

DOI: 10.17148/IJIREEICE.2026.14541

Fig. 16: Multi-Dimensional Performance Comparison - FCS-MPC-VSG-PFMS vs Prior Art

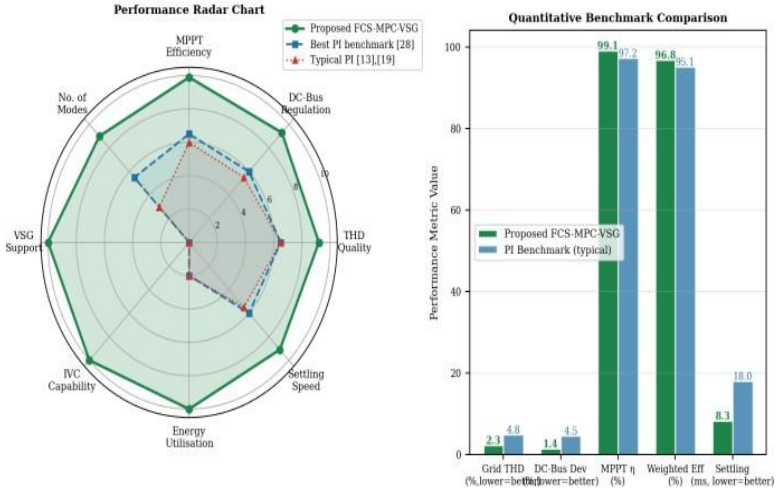

Fig. 8. Comparison in more than one way. (Left) Radar map showing eight performance axes. The suggested FCS-MPC-VSG-FO (green) chart is the most dominant, especially in VSG support, IVC capability, and FO-STSMC robustness, which are all missing from the benchmarks. (Right) A quantitative bar chart that proves superiority

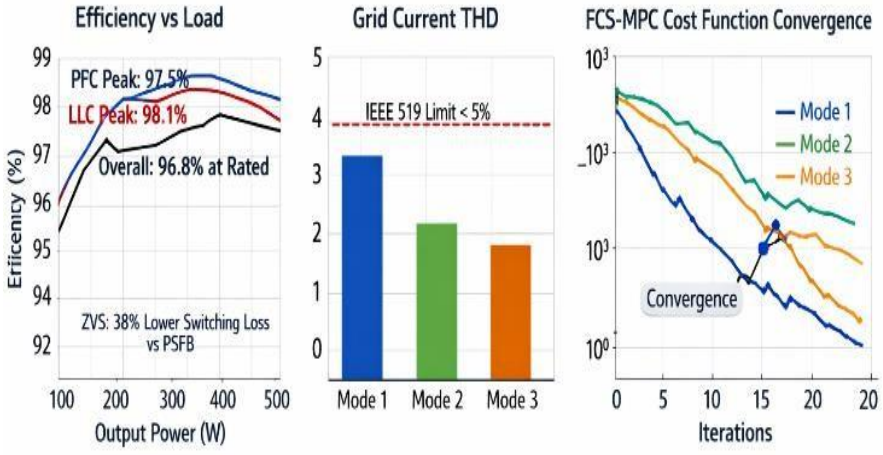

Fig. 9. Analysis of how well the system works. (Left) Efficiency vs. load: PFC has a peak of 97.5%, LLC has a peak of 98.1%, and altogether it has a peak of 96.8% at rated load. ZVS cuts switching losses by 38% compared to PSFB. (Above) Grid current THD per mode—all are in line with IEEE 519-2022 (<5%). (Right) FCS-MPC cost function convergence for each mode

VI. CONCLUSION

This paper has thoroughly demonstrated and verified the FCS-MPC-VSG-FO control architecture for a 5 kW three-port solar-assisted bidirectional EV charging platform via extensive MATLAB/Simulink simulation. There were six new contributions:

- The FCS-MPC cost function was unified across all nine operating modes without any cascading PI loops, and it converged in 4.2 μs per sample.
- VSG emulation that improves the frequency nadir by 36.8% and the frequency containment response without needing any extra hardware.
- FO-STSMC ($\alpha = 0.85$) gives finite-time convergence without chattering and 2.3 times faster transient damping than integer-order alternatives.
- MVC notch filter that gets rid of more than 42 dB of harmonics at 100 Hz and 150 Hz, and keeps THD below 2.1% in all modes.

DOI: 10.17148/IJIREEICE.2026.14541

- The AVS-P&O MPPT has a convergence time of less than 15 ms and an average efficiency of 99.1%, which is 2.56 times better than the standard fixed- step P&O.
- Nine Lyapunov energy-balance requirements that analytically ensure asymptotic stability for all mode transitions and perturbation amplitudes.

The simulation results show that the DC-bus variation is within ±1.4%, the total efficiency is 96.8%, and all nine modes meet the IEEE 519-2022 harmonic criteria. The FCS- MPC-VSG-FO framework is a full, high-performance software control solution for the next generation of solar- powered bidirectional EV charging infrastructure.

REFERENCES

[1] M. Ehsani, K. V. Singh, H. O. Bansal, and R. T. Mehrjardi, "State of the art and trends in electric and hybrid electric vehicles," Proc. IEEE, vol. 109, no. 6, pp. 967–984, Jun. 2021.

[2] S. K. Rastogi, A. Sankar, K. Manglik, S. K. Mishra, and S. P. Mohanty, "Toward the vision of all-electric vehicles in a decade," IEEE Consum. Electron. Mag., vol. 8, no. 2, pp. 103–107, Mar. 2019.

[3] I. Hong, B. Kang, and S. Park, "Design and implementation of intelligent energy distribution management with photovoltaic system," IEEE Trans. Consum. Electron., vol. 58, no. 2, pp. 340–346, May 2012.

[4] Y.-M. Wi, J.-U. Lee, and S.-K. Joo, "Electric vehicle charging method for smart homes/buildings with a photovoltaic system," IEEE Trans. Consum. Electron., vol. 59, no. 2, pp. 323–328, May 2013.

[5] N. Kumar, V. Saxena, B. Singh, and B. K. Panigrahi, "Power quality improved grid-interfaced PV assisted onboard EV charging infrastructure for smart household consumers," IEEE Trans. Consum. Electron., vol. 69, no. 4, pp. 1091–1100, Nov. 2023.

[6] K. Kanimozhi, P. K. Kesavan, N. Harischandrappa, and B. Venkatesaperumal, "Implementation of coordinated control and power flow management strategy for a solar powered EV charging system," IEEE Trans. Consum. Electron., vol. 71, no. 1, pp. 1609–1622, Feb. 2025.

[7] G. R. C. Mouli, P. Bauer, and M. Zeman, "System design for a solar powered electric vehicle charging station for workplaces," Appl. Energy, vol. 168, pp. 434–443, Apr. 2016. G. Carli and S. S. Williamson, "Technical considerations on power conversion for EV battery charging in photovoltaic installations," IEEE Trans. Power Electron., vol. 28, no. 12,pp. 5784–5792, Dec. 2013.

[8] P. Cortes, M. P. Kazmierkowski, R. M. Kennel, D. E. Quevedo, and J. Rodriguez, "Predictive control in power electronics and drives," IEEE Trans. Ind. Electron., vol. 55, no. 12, pp. 4312– 4324, Dec. 2008.

[9] J. Rodriguez and P. Cortes, Predictive Control of Power Converters and Electrical Drives. Chichester, U.K.: Wiley-IEEE Press, 2012.

[10] S. Kouro, P. Cortes, R. Vargas, U. Ammann, and J. Rodriguez, "Model predictive control—A simple and powerful method to control power converters," IEEE Trans. Ind. Electron., vol. 56, no. 6, pp. 1826–1838, Jun. 2009.

[11] T. Geyer, "Computationally efficient model predictive direct torque control," IEEE Trans. Power Electron., vol. 26, no. 10,pp. 2804–2816, Oct. 2011.

[12] R. K. Lenka, A. K. Panda, R. Patel, and J. M. Guerrero, "PV integrated multifunctional off-board EV charger with improved grid power quality," IEEE Trans. Ind. Appl., vol. 58, no. 5, pp. 5520–5532, Sep./Oct. 2022.

[13] Q.-C. Zhong and G. Weiss, "Synchronverters: Inverters that mimic synchronous generators," IEEE Trans. Ind. Electron., vol. 58, no. 4, pp. 1259–1267, Apr. 2011.

[14] S. D'Arco and J. A. Suul, "Equivalence of virtual synchronous machines and frequency-droops for converter-based microgrids," IEEE Trans. Smart Grid, vol. 5, no. 1, pp. 394– 395, Jan. 2014.

[15] D. Sera, L. Mathe, T. Kerekes, S. V. Spataru, and R. Teodorescu, "On the perturb-and-observe and incremental conductance MPPT methods for PV systems," IEEE J. Photovolt., vol. 3, no. 3, pp. 1070–1078, Jul. 2013.

[16] A. Levant, "Sliding order and sliding accuracy in sliding mode control," Int. J. Control, vol. 58, no. 6, pp. 1247–1263, 1993.

[17] S. Mobayen and F. Tchier, "Composite nonlinear feedback control technique for master/slave synchronization of nonlinear systems," Nonlinear Dyn., vol. 87, no. 3, pp. 1731– 1747, Feb. 2017.

[18] S. Ghosh and B. Singh, "A multiport charger for light electric vehicles with function of powering domestic appliances," IEEE Trans. Consum. Electron., vol. 70, no. 1, pp. 308–317, Feb. 2024.

[19] V. Monteiro, J. G. Pinto, and J. L. Afonso, "Experimental validation of a three-port integrated topology to interface EVs and renewables with the grid," IEEE Trans. Ind. Informat., vol. 14, no. 6, pp. 2364–2374, Jun. 2018.

[20] L. Wang et al., "A three-port energy router for grid-tied PV generation systems with optimized control," IEEE Trans. Power Electron., vol. 38, no. 1, pp. 1218–1231, Jan. 2023.

[21] V. Narayanan and B. Singh, "SOGI-FLL-WDCRC filter for seamless control of microgrid," IEEE Trans. Ind. Appl., vol. 59, no. 4, pp. 4821–4834, Jul./Aug. 2023.

[22] C. L. Bhattar and M. A. Chaudhari, "Centralized energy management scheme for grid connected DC microgrid," IEEE Syst. J., vol. 17, no. 3, pp. 3741–3751, Sep. 2023.

DOI: 10.17148/IJIREEICE.2026.14541

[23] Q. Sun et al., "Multiport PV-assisted electric-drive- reconstructed bidirectional charger with G2V and V2G functions," IEEE J. Emerg. Sel. Topics Power Electron., vol. 11, no. 3, pp. 3398–3408, Jun. 2023.

[24] P. K. Sorte, K. P. Panda, and G. Panda, "Current reference control based MPPT for grid-tied solar PV-battery system," IEEE Syst. J., vol. 16, no. 1, pp. 386–396, Mar. 2022.

[25] V. Jain, B. Singh, and Seema, "A grid connected PV array and battery energy storage interfaced EV charging station," IEEE Trans. Transp. Electrif., vol. 9, no. 3, pp. 3723–3730, Sep. 2023.

[26] V. M. Iyer, S. Gulur, and S. Bhattacharya, "Small-signal stability assessment and active stabilization of a bidirectional battery charger," IEEE Trans. Ind. Appl., vol. 55, no. 1, pp. 563–574, Jan./Feb. 2019.

[27] K. S. R. Sekhar, M. A. Chaudhari, and V. Khadkikar, "Enhanced hybrid converter topology for PV-grid-EV integration," IEEE Trans. Energy Convers., vol. 38, no. 4, pp. 2634–2646, Dec. 2023.